Research Article | Vol. 31, No. 18 / 28 Aug 2023 / Optics Express 29213
Optics EXPRESS

On-chip multi-beam frequency shifter through sideband separation

EMIEL DIEUSSAERT,[1,2,*] ROEL BAETS,[1,2] AND YANLU LI[1,2]

[1] Photonics Research Group, Ghent University-imec, Technologiepark 126, 9052, Ghent, Belgium
[2] Center for Nano- and Biophotonics, Ghent University, Technologiepark 126, 9052, Ghent, Belgium
[*] Emiel.Dieussaert@ugent.be

Abstract: In this paper, we introduce a novel method to realize a multi-beam optical frequency shifting component for photonic integrated circuits, utilizing an array of parallel optical modulators and a free-propagation region (FPR), such as a slab waveguide-based star coupler. This component generates multiple optical beams with different frequency shifts, making it suitable for various systems, such as multi-beam laser Doppler vibrometry (LDV). We thoroughly elaborate on the working principle of the component through theoretical analysis and demonstrate that by applying periodic wave-like modulation in the modulator array, the discrete harmonic content of the light can be selectively directed to different outputs based on the delay between consecutive modulators. A design comprising a 16-element modulator array and 5 outputs will be presented. Simulations show that this design can generate and collect 5 different harmonics (−2, −1, 0, +1, +2) in the different outputs with a side band suppression ratio of 20 dB to 30 dB for each output. Our proposed design is just one possibility and the component can be modified and optimized for specific applications.

1. Introduction

Surface vibration detection is an important technique for various applications, such as non-destructive testing (NDT) and photoacoustic imaging. In these applications, there is a growing demand for multi-point or full-field detection to achieve more comprehensive detection of the target [1,2]. Current full-field measurements primarily rely on camera-based optical interferometry (e.g., shearography [3]). However, these techniques are often limited by the detection bandwidth [4], making them less suitable for detecting vibrations with larger amplitudes (which cause large Doppler shifts) or higher frequencies. Laser Doppler vibrometry (LDV) enables higher bandwidth single-point vibration measurements but is limited by detection points. Full-field detection with LDV requires scanning sensing beams over the surface, effective only for repetitive vibrations and entails lengthy measurements. Significantly increasing the number of sensing beams in LDV systems enhances full-field measurement capabilities, allowing for more accurate detection of complex vibration patterns and dynamic behaviors.

Advancements in photonic integrated circuit (PIC) techniques [5], especially in silicon photonics, enable compact, cost-effective multi-channel LDV systems compared to systems based on discrete optical components [1,6]. Therefore, the PIC technique is a promising candidate for enabling improved full-field detection systems. However, in practice, as the number of sensing beams increases, the PIC space still needs to be considerably expanded. The increased number of sensing channels adds complexity to packaging and readout electronics, making PIC-based full-field measurements highly challenging. Additionally, current PIC-based LDVs use the homodyne detection method rather than the heterodyne method employed by commercial LDVs [7]. Although the heterodyne technique has been proven to improve the performance of LDV systems in many situations [8–10], the key component to enable the heterodyne technique, i.e. the optical frequency shifter, is not yet fully available in silicon PICs. Several possible options have been reported: (1) The serrodyne technique uses sawtooth-shaped phase modulation to generate

#498792 https://doi.org/10.1364/OE.498792
Journal © 2023 Received 26 Jun 2023; revised 4 Aug 2023; accepted 7 Aug 2023; published 16 Aug 2023

Optics EXPRESS

a single sideband output, but it suffers from modulator nonlinearities and limited bandwidth [11,12]. (2) IQ modulators, which use two Mach Zehnder modulators driven by cosine and sine signals with a $\pi/2$ phase difference, can also produce a single sideband output [13–15]. These IQ frequency shifters are less sensitive to modulator non-linearities and more suitable for generating high-frequency shifts. However, using these frequency shifters for simultaneous full-field detection is nearly impossible, considering both system space and cost. The proposed method of this paper aims to address these issues.

For free-space LDVs, it has been shown that synthetic-array heterodyne detection can decrease the size and the cost of a multi-beam LDV system [16,17]. In this technique, each sensing beam is frequency-shifted to a different carrier with AOMs. After reflection of the test object, they are combined with the local oscillator on a photodetector, through which the sensing signals and carrier frequency are transferred to the electrical domain, where the different sensing beams can be distinguished through the different carrier frequencies. The multiplexed electrical signals can be amplified and recorded by the same circuit. This technique also helps to reduce crosstalk between different sensing beams, thanks to the separation in the frequency domain, compared to multi-beam homodyne systems. While free-space circuits have successfully utilized Acousto-Optic Modulators (AOMs) in the Raman-Nath regime as multi-beam frequency shifters [16–19], and acousto-optic modulators have been demonstrated on various platforms [20–23], on-chip acousto-optic multi-beam frequency shifters are still notably absent from most commercial Silicon-On-Insulator (SOI) platforms. The implementation of such a feature requires the heterogeneous integration and processing of suitable acousto-optic materials, which consequently increases complexity and cost.

This paper proposes a novel method to generate a multi-beam frequency shifter in the SOI platform. Serving as a frequency shifter, the approach holds value for diverse applications, including optical communications [24,25], remote sensing [26], velocimetry [27] and microwave photonics [28]. When incorporated into PIC-based LDV systems, it breaks through existing constraints, allowing simultaneous multi-beam, and potentially, full-field measurements. This paper delves into the theory of Raman-Nath modulation and proposes the use of an array of discrete modulators to create on-chip solutions for creating multiple heterodyne beams by mimicking the wave-like acoustic modulation properties. Hereby eliminating the need for materials with good acousto-optic properties to be integrated into the silicon platform and offering better control over modulation than AOMs, enabling fine-tuned output harmonics. We also discuss design considerations and present a simulated structure utilizing a star coupler for the efficient separation of different modulation orders. Our approach has the potential to significantly reduce the size and cost of on-chip multi-beam LDV systems and expand the capabilities of photonic integration.

2. Theoretical framework

2.1. Interaction of light with wave-like modulations

In this section, we will discuss the interaction between optical waves and a traveling modulation wave with a short interaction length, similar to an AOM in the Raman Nath diffraction regime [18,19]. As depicted in Fig. 1(a), let us consider a two-dimensional scenario where a monochromatic optical plane wave is expressed in complex notation as $U_i(x,z,t) = A_i \exp(j2\pi f_0 t - j\mathbf{k_0}\mathbf{r})$, with A_i denoting the amplitude, f_0 as the optical frequency, t as time, $\mathbf{r}$ as the position vector, $\mathbf{k_0} = k_{0x}\hat{\mathbf{x}} + k_{0z}\hat{\mathbf{z}}$ as the k-vector of the optical beam, $\hat{\mathbf{x}}$ and $\hat{\mathbf{z}}$ represent the unit vector in the x and z directions, respectively. Here the k-vector fulfills the following relation: $|\mathbf{k_0}| = 2\pi/\lambda$, where λ is the optical wavelength of light in the medium. As shown in Fig. 1(a), let us examine an acoustic wave with a negligible width L (operating in the Raman-Nath diffraction regime), traveling along the x axis ($z = 0$) and modulating the optical wave through the photo-elastic effect.

Right after the modulation, the optical wave can be expressed as $U_m(x,t) = U(x, z = 0^+, t) = M(x,t)U_i(x, z = 0^-, t)$, where $M(x,t)$ is the modulation applied by the acoustic wave. When the

Optics EXPRESS

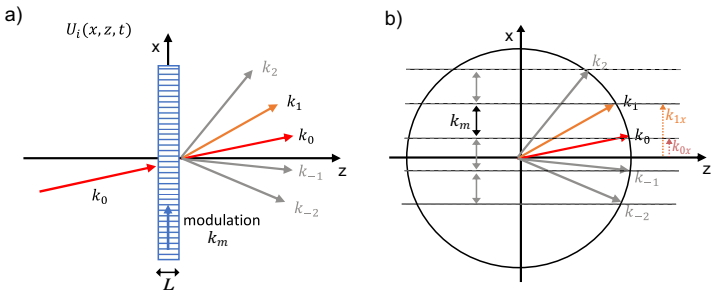

Fig. 1. (a) A 2D propagating optical wave interacting with a wave-like modulation, represented by wave vector k_m, traveling along the x-axis resulting in scattering to a different direction. In grey, the scattering into different discrete directions due to a periodic wave-like modulation, similar to an AOM (b) k-vector diagram of the modulated wave vectors.

traveling acoustic wave maintains a constant velocity v, the modulation can be expressed as a wave-like function $M(x,t) = W(x - vt)$. Considering the Fourier expansion of the modulation function $W(x)$ in the x direction is given by

$$W(x) = \int_{-\infty}^{+\infty} W^F(k_x) \exp(-jk_x x) dk_x, \tag{1}$$

the modulated optical wave can be expressed as an angular decomposition of plane waves through Fourier optics.

$$\begin{aligned} U_m(x,t) &= A_i e^{j2\pi f_0 t} \exp(-j2\pi k_{0x} x) W(x - vt) \\ &= A_i \int_{-\infty}^{+\infty} W^F(k_x) \exp(j2\pi[f_0 - \frac{k_x v}{2\pi}]t) \exp(-j[k_{0x} + k_x]x) dk_x \end{aligned} \tag{2}$$

From this equation, it is evident that the modulated optical field is scattered in different directions due to the modulation wave. Assuming the propagation direction of a scattered component is described by $\mathbf{k}' = k_x'\hat{\mathbf{x}} + k_z'\hat{\mathbf{z}}$, the following relations should be fulfilled.

$$\begin{aligned} k_x' &= k_{0x} + k_x \\ |\mathbf{k}| &= 2\pi/\lambda \end{aligned} \tag{3}$$

Figure 1(a), depicts the interaction between an optical monochromatic wave and a modulated traveling wave and it shows the scattering in a different direction (in color). As can be seen in Fig. 1(b), the relations from Eq. (3) hold. In the figure, k_x' is represented by k_1 and the added vector due to modulation (k_x in Eq. (3)) is represented by k_m. In grey, the scattering into different discrete directions due to a periodic wave-like modulation, similar to an AOM is depicted, which will be explained in a following section (Section2.2).

The phasor corresponding to this component is $A_i W^F(k_x) \exp(j2\pi(f_0 - \frac{k_x v}{2\pi})t)$, showing that, when the modulation wave is propagating in the x direction with a constant speed v, the angular frequency shifts in the x direction k_x and the temporal frequency shifts Δf_t of the scattered light are always correlated through the equation

$$\Delta f_t = -\frac{k_x v}{2\pi}. \tag{4}$$

Optics EXPRESS

2.2. Periodic modulation

Considering the wave-like modulation function $W(x - vt)$ to be periodic, which is denoted as $W_p(x - vt)$. It is possible to define a spatial and temporal period P and T

$$\begin{aligned} W_p(x - vt) &= W_p(x - vt + P) \\ &= W_p(x - v(t + T)) \quad \text{with} \quad T = P/v \end{aligned} \tag{5}$$

Define $a(x)$ to be the single period of $W(x)$

$$a(x) = \begin{cases} W(x), & \text{if } 0 \le x < P \\ 0, & \text{otherwise} \end{cases} \tag{6}$$

Thanks to the periodicity, the Fourier expansion of the modulation can now be written as a discrete sum

$$W_p(x - vt) = \sum_{n=-\infty}^{+\infty} a^F(\frac{2\pi n}{P}) \exp(-j\frac{2\pi n}{P} vt) \exp(-j\frac{2\pi n}{P} x), \tag{7}$$

where $a^F(k_x)$ denotes the Fourier components of the plane-wave decomposition of $a(x)$. With the same procedure used in the previous section, the scattered optical field can now be decomposed in discrete spatial frequencies.

$$U_m(x, t) = A_i \sum_{n=-\infty}^{+\infty} a^F(n\frac{2\pi n}{P}) \exp(j2\pi(f_0 - \frac{n}{P}v)t) \exp(-j(k_{0x} + \frac{2\pi n}{P})x) \tag{8}$$

As a result of the discrete expansion in plane waves, the light is scattered into discrete angles in the far field. According to the mapping relation in Eq. (4), different directions have different temporal frequency shifts.

These equations can describe the acoustic-optic interactions in the Raman-Nath regimes (short acoustic-optic interaction length).

2.3. Finite modulation region

In practice, the length of the modulation region (in the x direction) cannot be infinitely long. In order to account for the finite size of the incoming beam, the finite size of the modulation region, or the amplitude and phase differences along the modulation direction, we introduce a factor $G(x)$ in the system. The simplest case for $G(x)$ is a rectangle function which is zero everywhere except for the finite modulation region. The modulation function can be written as

$$M(x, t) = G(x)W(x - vt). \tag{9}$$

Since the angular frequency spectrum of the scattered field is proportional to the Fourier transform of $M(x)$, it can be described as the convolution between the plane-wave expansion of $G(x)$ and the Fourier expansion of $W(x - vt)$. In this case, the mapping relation between the wave vectors and temporal frequency shifts (Eq. (4)) is not strictly valid anymore. However, if $G(x)$ describes a curve that is relatively wide such that in the angular frequency domain it has a small angular bandwidth, Eq. (4) can still be used as a large field approximation. In the case of periodic modulations, the discrete frequency components will mix unless the width of $G(x)$ is big enough to ensure the minimal beam size of the scattered light is smaller than the angular separation of the discrete beams. When $G(x)$ breaks the large field approximation, numerical methods can be used to analyze the scattered fields.

Optics EXPRESS

2.4. Discrete modulator array and coupling to free propagation region

While considerable advancements have been made in incorporating acousto-optic materials onto the silicon photonics platform [23], these additions necessitate extra processing steps beyond most commercially available silicon photonic platforms, leading to higher costs and increased complexity. In this context, we propose a discrete modulator array coupled to a Free Propagation Region (FPR) as an alternative solution for achieving wave-like modulation. Figure 2(a) shows a possible on-chip layout of a discrete modulator array coupled to an FPR through a grating with spacing Λ. We aim to replicate the characteristics of diffracted light under acoustic modulation by coupling wave-like modulated light of this array to an FPR.

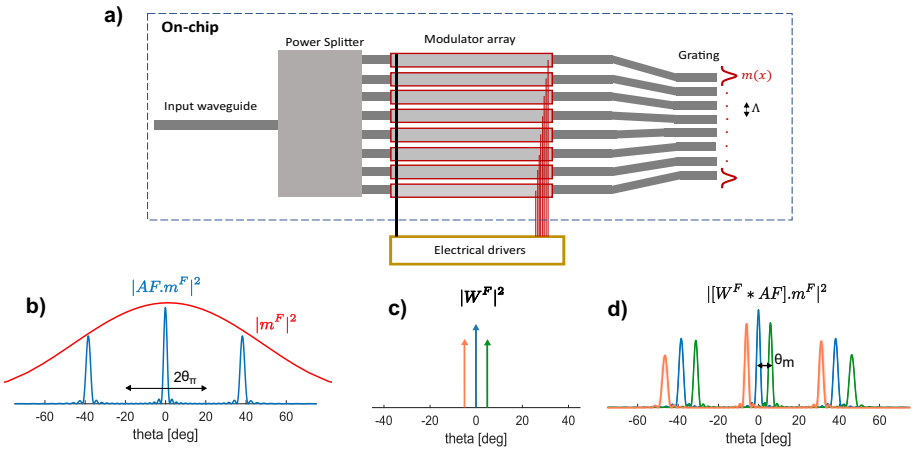

Fig. 2. (a) Schematic of a modulator array connected to a grating array with spacing Λ and element field profile $m(x)$. (b) In red: the far field pattern m^F of a single element with a rectangular field profile $m(x)$ with $width = 800\ nm$. In blue; the angular intensity profile of the passive array grating of 16 elements with equal amplitude and phase. (c) Output of a plane wave modulated in periodic traveling-wave-like fashion resulting in discrete output angles with each having a different frequency shift compared to the central beam. Here only the $\pm 1^{st}$ order sidebands were considered. (d) Combining the traveling-wave-like modulation technique and the passive array grating output, an angular output spectrum which is the convolution of (b) and (c) is obtained.

First, the properties of a 1D linear phased array grating and its coupling to an FPR are discussed. Subsequently, the theory of wave-like modulation is combined with the grating array properties to design multi-beam frequency shifters based on discrete modulator arrays.

An array grating serves to convert phase and intensity relations between discrete elements into a specific far-field pattern after propagating through an FPR. While various forms of optical arrayed gratings exist, we focus on a 1D linear array for simplicity. Consider a 1D linear array of N elements with field profile $m(x)$ (and $m^F(k_x)$ its spatial Fourier transform), spaced with a period of Λ along the x-axis, similar to the grating depicted in Fig. 2(a). Considering equal amplitude elements, but a linear phase shift $\Delta\psi$ between consecutive elements, we can write for the field at

Optics EXPRESS

the x-axis (with $'*'$ representing convolution):

$$\begin{aligned} U_m(x,t) &= \sum_{n=0}^{N} [A_i \exp(j(2\pi f_0 t - n\Delta\psi))\delta(x - n\Lambda)] * m(x) \\ &= \left[A_i \exp(j(2\pi f_0 t - k_{0x}x)) \sum_{n=0}^{N} \delta(x - n\Lambda)\right] * m(x) \quad \text{with} \quad k_{0x} = \Delta\psi/\Lambda \\ &= A_i \exp(j2\pi f_0 t) \int_{-\infty}^{+\infty} AF(k_x, \Lambda) m^F(k_{0x} + k_x) \exp(-j(k_{0x} + k_x)x) dk_x \end{aligned} \tag{10}$$

where AF is the array factor of a 1D linear array grating $AF(k_x, \Lambda) = \sum_{n=0}^{N} \exp(-jnk_x\Lambda)$.

The Fourier transform of the element field profile, multiplied by the grating array factor, results in the angular decomposition after a periodic, finite grating. Figure 2(b) presents the angular intensity profile of a 16-element linear array grating (blue) derived from the modulus squared of the single-element Fourier transform (red) multiplied by the array factor. We used a wavelength $\lambda = 1550\ nm$, pitch $\Lambda = 2.5\ \mu m$, and approximated each element's field profile using an 800 nm width rectangular function. In Fig. 2(b) we assumed no linear phase shift to be present ($\Delta\psi = 0 \rightarrow k_{0x} = 0$) such that $2\pi k'_x = \sin(\theta)/\lambda$. The indicated $2\theta_\pi$-region in the figure represents the 0_{th} order diffraction region when scanning with the phased array grating with a consecutive phase delay $\Delta\psi$ between $-\pi$ and π. This region will be important when designing the grating structure.

A linear phase shift $\Delta\psi$ between consecutive elements induces a shift of the array factor enabling light direction tuning via a linear phased array. The 0^{th} grating order's output angle can be estimated with $\sin(\theta) = \frac{\Delta\psi}{\Lambda}\frac{\lambda'}{2\pi}$, where λ' refers to the wavelength in the FPR and θ the angle between the z-axis and the propagation direction.

In Eq. (10), we assumed identical field amplitude and linear phase shift for each element and linear phase shift. Now, we include wave-like modulation factor $W(x - vt)$, which modulates each element according to the wave-like character.

$$U_m(x,t) = A_i \int_{-\infty}^{+\infty} e^{j2\pi(f_0 - k_x v)t} [W^F * AF](k_x) m^F(k_{0x} + k_x) e^{-j(k_{0x} + k_x)x} dk_x. \tag{11}$$

With Eq. (11), the expected far field of this array under periodic and traveling-wave-like modulation can be calculated numerically. Figure 2(c), shows the angular field pattern of a monochromatic wave ($\lambda = 1550\ nm$) along the z-axis, scattered by a periodic wave-like modulation with a fundamental frequency of 1 MHz and a velocity of 14.76 m/s along the x-axis (for simplicity we assume only scattering to ± 1 harmonic). In this example, the ± 1 harmonics are scattered to around $\theta_m = +6^\circ$ and -6° (see Eq. (4)). Considering the 16-element linear array with period $\Lambda = 2.5\ \mu m$ and a wavelength of 1550 nm, this wave-like modulation can be emulated by connecting the linear array to a modulator array (as shown in Fig. 2(a) with a linear phase shift $\Delta\psi = \pi/3$ between the modulation of the modulators respectively.

Equation (11) tells us how to combine the results from Fig. 2(b) and (c) to yield the resulting far-field pattern in Fig. 2(d), it can be seen that by using a modulator array connected to a discrete array coupled to an FPR and emulating wave-like modulation, different discrete frequency shifts can be generated and separated in the FPR, which allows designing multi-beam frequency shifters. The $2\theta_\pi$-region, determined by the grating period, and θ_m determined by the modulation and delay between modulators in consecutive arms, are two important parameters to consider during the design stage for a multi-beam frequency shifter.

3. Design

In the previous section, we discussed the potential for using a combination of a modulator array and a phased array grating to generate multiple discrete frequency-shifted beams with different

Optics EXPRESS

propagation directions. Instead of using a straight optical phased array (Fig. 2(a)) that projects light into the far field, one can use a curved optical phased array to focus the light, where it can be collected through output waveguide apertures [29]. These curved optical phased arrays, or star couplers, allow for designing a multi-beam frequency shifter on a compact chip. Figure 3 shows a schematic where a single frequency input is distributed across a waveguide array, and, after modulation, light is coupled from input apertures into an FPR (e.g. a slab waveguide). There, the different harmonics are directed to output waveguides at the end of the FPR. By using the modulator array to mimic the properties of a Raman-Nath acousto-optic modulator, as described earlier, different single sideband frequency-shifted beams can be directed to the output of each waveguide. In the following sections, we will examine the key design considerations for creating a frequency-shifting structure using a modulator array and an FPR.

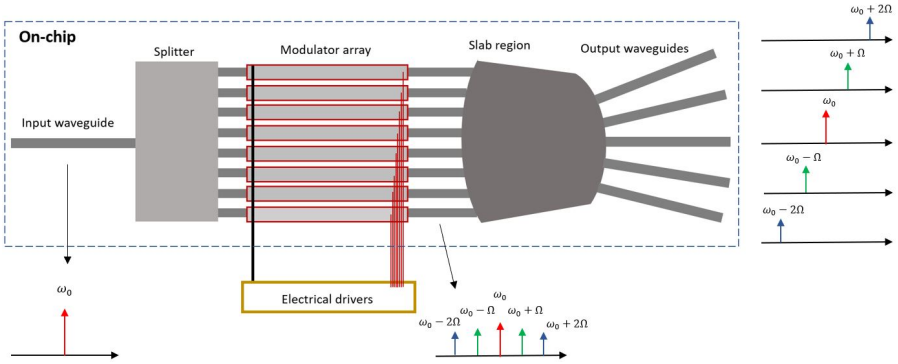

Fig. 3. Schematic of an on-chip heterodyning component using a star coupler to separate the different beams generated through the traveling-wave-like modulation of the modulator array.

3.1. Modulation

As described in Section 2, the modulation dictates the frequency content of the light relative to the baseband frequency. Periodic modulation disperses power across different discrete harmonics. Thus, the characteristics and waveforms of the modulator are crucial considerations. The silicon photonics platform has seen the development of a broad range of modulation techniques and devices, including but not limited to micro-electro-mechanical systems (MEMS), thermo-optic modulators, free carrier dispersion modulators, and electro-absorption modulators [30,31]. These devices enable amplitude and/or phase modulation with various characteristics and at different modulation frequencies. To provide a non-exhaustive exploration of various possibilities, we examine perfect phase modulation with different special modulation waveforms, a sine-driven pn-modulator, and amplitude modulation.

In Fig. 4, we look at these different modulations. As can be seen from Fig. 4(a)-(c), pure sine phase modulation gives rise to multiple sidebands, depending on the amplitude of the modulation. Figure 4(c) shows the output spectrum for a pure sine phase modulation with modulation depth $r = 1.84$, which maximizes the amplitude of the -1^{st} and 1^{st} harmonic, as can be seen from 4(b). Figure 4(d)-(f) shows results as expected from a 5-mm long pn-modulator, modeled using the description of the plasma dispersion effect from Soref and Bennett [32]. The 5 mm pn-modulator has considerable insertion loss and we can see some small amplitude modulation apart from the larger phase modulation. Note that amplitude modulation is not detrimental to the working principle of the proposed design. To increase the number of sidebands in Fig. 4(f), one should apply higher voltages or increase the modulator length, but this increases the overall power loss.

Optics EXPRESS

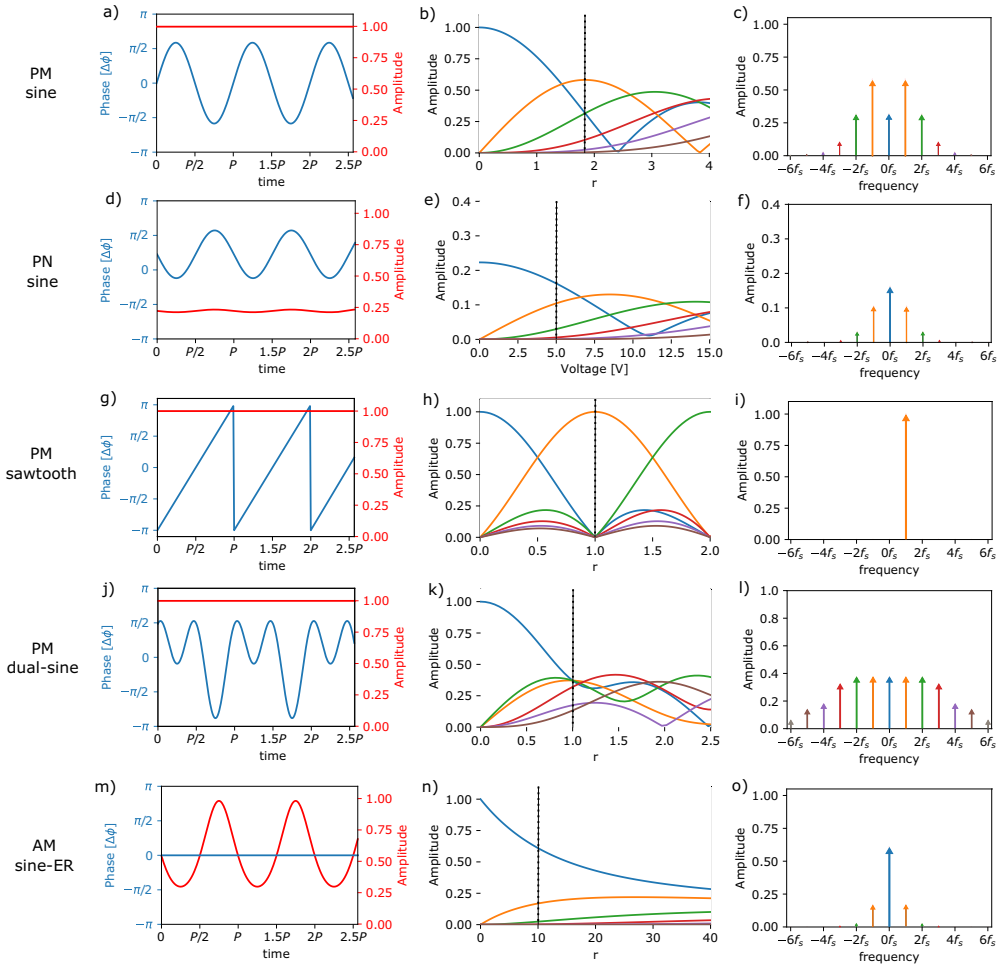

Fig. 4. Different modulations can yield different interesting harmonic content. Each row depicts the figures for one type of modulation. The figure in the first column shows the modulation waveform. The second column shows the influence of the change in the amplitude of that specific modulation and the third column shows the amplitude spectrum of the modulation depicted in the first column and highlighted with the dotted line in column 2. (a) to (c) considers pure sine phase modulation (PM-sine) whereby $\Delta\phi = r \cdot \sin(\omega_s t)$. (d) to (f) considers the 5 mm long pn-modulator driven by a voltage sine signal (PN-sine). (g) to (i) considers sawtooth phase modulation with amplitude of the phase modulation=$r \cdot \pi$. (PM-sawtooth) (j) to (l) shows a dual sine phase modulation with phase modulation described as $\Delta\phi = r \cdot [1.24 \sin \omega_s t + 1.53 \sin(\omega_s t + \pi/2)]$, resulting in an equalized output for the first five harmonics for r=1 (PM - dual sine). (m) to (o) depicts amplitude modulation driven by a sine signal (AM sine-ER) and where the extinction ratio is linear with the applied voltage yielding an amplitude modulation of $A = 10^{-r/20 \cdot (1+sin\omega_s t)}$.

In Fig. 4(m)-(o), we show results for pure amplitude modulation whereby the extinction ratio is linear with the applied voltage, (approximating the behavior of electro-absorption modulators). It is clear that amplitude modulation can also be used for sideband creation, but absorption-based modulators are fundamentally less power efficient compared to lossless phase modulators.

Other special modulations are possible and can yield interesting results. Figure 4(g)-(i) and Fig. 4(j)-(l) show special cases for pure phase modulation. Sawtooth phase modulation with an

Optics EXPRESS

amplitude covering a 2π phase modulation results in a single sideband output. This serrodyne technique creates one single frequency shifted beam but requires high bandwidth of the driving electronics and modulator [11,12]. It has been proven that using dual or more sine phase modulations can equalize comb amplitudes (for a number of combs) [33,34]. Figure 4(j)-(l) show dual sine phase modulation giving rise to a comb profile with equalization of the 5 lowest order modes (−2,−1,0,1,2). Using different combinations of two or more sine phase modulations, one can equalize larger comb sizes.

In the following section, we will consider using pure sine phase modulators with a modulation depth of 1.84 (as denoted with the dotted line in Fig. 4(b) for creating a 16-by-5 multi-beam frequency shifter, collecting the harmonics between the -2^{nd} and $+2^{nd}$.

3.2. Star coupler and phased array design

In the past decade, there has been increasing interest in optical phased arrays due to their potential for non-mechanical beam-steering in applications such as remote sensing and free-space communication [35]. Recent efforts have focused on optimizing steering range, minimizing side lobes to increase beam steering efficiency, and demonstrating 2D arrays [35,36]. These optical phased arrays could be used to create a free-space coupled multi-beam frequency shifter, provided each element can be modulated with wave-like modulation relative to each other, as described in Section 2. However, in this paper, we focus on the development of a multi-beam frequency shifter that does not couple into free space. Instead, we employ a star coupler to propagate and collect the frequency-shifted beams on-chip.

For a star coupler design, the input grating follows a circular arc, creating a circular phase front focusing on the center of the circle when no phase difference is present between the input waveguides. Introducing a phase difference between consecutive elements creates a shift of the focal point, which will move along a new circle with half the radius, called the Rowland circle. Now, by taking into account the number of output apertures, one can start determining the different parameters of the star coupler.

Consider, one chooses to collect or use M output waveguides. For a star coupler design, it is important to position the output waveguides in agreement with the expected diffracted angle of the harmonics to be collected. It is however possible to tune the separation between the diffraction angles by changing the delay of modulation between consecutive modulators.

When considering modulation by applying a sine signal or any other symmetric signal, the distribution across the harmonics is symmetric. Without an angular shift applied, a symmetric output design where the harmonics between -(M-1)/2 and +(M-1)/2 are captured or used, can result in a power-efficient system. For such a system, we follow the general design guidelines for an N-by-M star coupler. The number of input apertures N is important for the efficiency of coupling to the output apertures, generally one uses at least N>3M input apertures for M output channels [29]. First, the spreading angle of the star coupler output aperture can be calculated by looking at the far-field projection. The N input apertures should be distributed within the spreading angle for efficient power coupling and results in a minimum for the radius of the Rowland circle.

Schematic in Fig. 5(a) shows the important parameters to consider for the star coupler design. From the period of the N input apertures, we can estimate the $2\theta_\pi$ region; it is the angle scanned by the 0^{th} order diffraction for the phased array with the phase delay $\Delta\psi$ scanned from $-\pi$ to π. The M output apertures should fit within $2\theta_\pi$ region while staying away from the edges of this region. Otherwise, the M^{th} harmonic might overlap with output waveguides.

With these considerations in mind, the minimal grating radii of the star coupler can be calculated. To arrange M output waveguides, an initial approach would be to choose the angular separation to be equal and approximately $\theta_s = 2\theta_\pi/(M+1)$. This choice ensures the collection of different harmonics while preventing the $\pm((M+1)/2)$ harmonics from overlapping with any

Optics EXPRESS

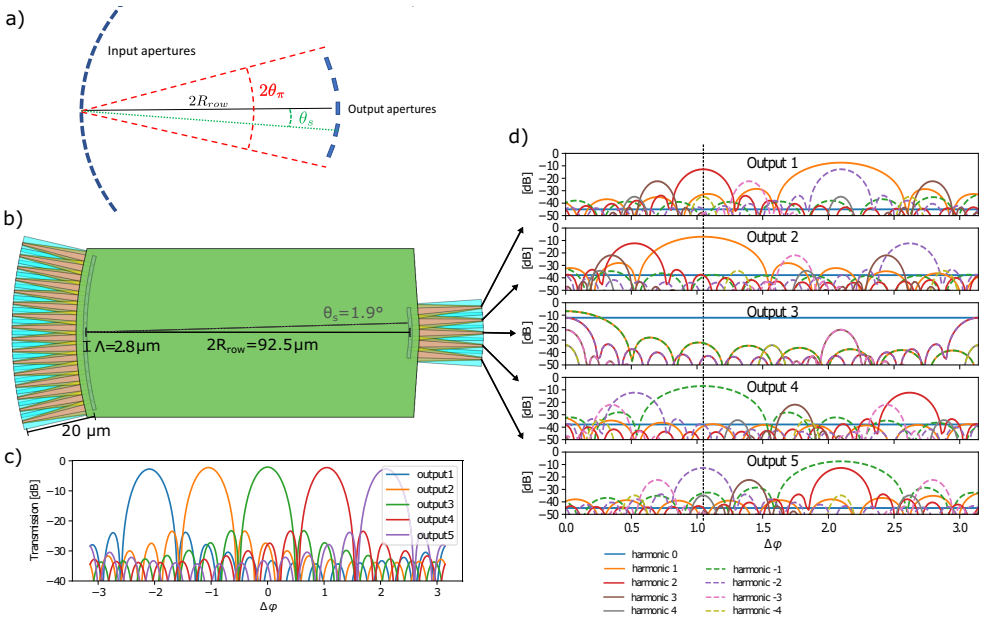

Fig. 5. (a) Schematic of the layout of the star coupler with important design parameters; the diameter of the Rowland circle, which is the distance between the in- and output apertures $2R_{row}$, the spreading angle θ_s and 0^{th} order diffraction angle $2\theta_\pi$. (b) Design of the 16-by-5 starcoupler. (c) The transmission to different outputs of the 16-by-5 star coupler, with equally distributed input in the function of the phase difference between consecutive inputs. (d) Resulting output power of the different harmonics into different ports when using pure sine phase modulation with depth 1.84 for different delays between the consecutive modulators.

output. However, higher harmonics might overlap with the outputs. If this overlapping becomes an issue, for instance, when using modulation with power in these higher harmonics, it can be mitigated by decreasing the angular separation. This will be further elaborated in Section 4.

After determining different parameters, the design and performance can be estimated through simulation. Here, we first calculate the s-matrix of the star coupler using the IPKISS AWG designer [37]. Apertures are simulated using CAMFR [38], doing 1D mode solving and 2D eigenmode expansion propagation. The propagation through the FPR is calculated through the Rayleigh Sommerfeld diffraction expressions. Modal overlaps are used for calculating power coupling into the waveguides. Here, a 220 nm thick silicon platform is considered, resembling commercially available silicon photonic platforms [39]. Following the guidelines described in this section, we designed a 16-by-5 star coupler with an input grating period of 2.8 μm. The design features a 20 μm linear taper structure from a single mode wire waveguide to the shallow-etched rib-wire apertures with a width of 2 μm and a Rowland circle radius equal to 46.25 μm (Fig. 5(b)). We set $\theta_s = 2\theta_\pi/6 = 1.9°$, as depicted in the design layout in Fig. 5(b). Figure 5(c) shows the transmission to the different ports, depending on the phase difference between the various arms. This is based on the scattering matrix while assuming equal power into every input arm and no modulation

As illustrated in Fig. 5(c), the outputs from the star coupler exhibit about −25 dB crosstalk to the neighboring outputs due to sidelobes. This crosstalk, along with the insertion loss from the star coupler, could be improved by increasing the aperture angle as viewed from the outputs [29], but this would necessitate the addition of more modulators to the star coupler.

Optics EXPRESS

Regarding fabrication challenges, minor changes in the effective index within the FPR could lead to different grating diffraction angles. This issue could be alleviated by tuning the angular spacing through changing the delay for consecutive modulators. However, this adjustment could inadvertently cause higher harmonics to overlap with the outputs, potentially degrading the suppression ratio, as will be elaborated in Section 4. If the higher harmonics do not carry significant power, as demonstrated in Fig. 5(d), this will not pose a problem.

DC phase errors due to path length differences or DC thermal crosstalk components can be compensated by thermo-optic phase shifters [40]. Thermal crosstalk between the elements and optical paths of the modulator array can however cause AC phase modulation to neighbouring elements (especially when using thermo-optic phase shifters for phase modulation [41]). Assuming a periodic, infinite array of modulators, every arm has the same influence such that the wave-like condition as described in 2.4 still holds. This concept can be expressed by considering the total modulation $M_i(t)$ in arm i. It can be formulated as a function f of the applied wave-like modulation W—as discussed in 2.4—along with the contributions from the modulations applied to the neighboring arms, which are separated by of Λ. We include however an arbitrary delay t_k, to account for the time delay of the thermal effect of the k^{th} neighbours.

$$\begin{aligned} M_i(t) = f\Big(&W[x_i - vt], W[x_i + \Lambda - v(t - t_1)], \\ &W[x_i - \Lambda - v(t - t_1)], \\ &W[x_i + 2\Lambda - v(t - t_2)], \dots\Big) \end{aligned} \tag{12}$$

From this, it is evident that when working with time-invariant systems, $M_i(t)$ can still be expressed as new a wave-like function:

$$M_i(t) = W'(x_i - vt). \tag{13}$$

This implies that thermal crosstalk will not affect the angular separation as discussed in 2. However, it will influence the modulation function and, as a result, the power distribution across the harmonics. In reality, the modulators at the edge will not have the same function, which could break the wavelike modulation. This edge effect can be mitigated by placing and modulating extra elements at the edges of the array.

4. Discussion

Considering a perfect sine phase modulator with modulation depth $r = 1.84$ (as defined in Fig. 4), the amplitudes of the harmonics behave as depicted in Fig. 4(a)-(c). Assuming this modulation results in Fig. 5(d), where it can be seen that the majority of the power will be contained in the 1^{st} and -1^{st} harmonic, while there will still be a substantial amount of power in the other captured harmonics.

In Fig. 5(c), the transmission of the star coupler is plotted, when the inputs have the same amplitude for different detunings of the phased array (without modulation). We can see optimal transmission in the different output ports at multiples of $\pi/3$. This is as expected since we chose

$$\theta_s = \frac{2\theta_\pi}{M+1} \xrightarrow{M=5} \frac{\theta_\pi}{3}. \tag{14}$$

Figure 5(d) shows the calculated output power of different harmonics for the multi-beam frequency shifter for sine phase modulation, with a modulation depth of around 1.84 (as was shown in Fig. 4(a-c)). The x-axis denotes the delay between consecutive modulations. It can be seen that for a delay of around $\pi/3$, we collect the 2^{nd} harmonic in the upper waveguide with

Optics EXPRESS

over 20 dB suppression of other harmonics. In the second output waveguide, we collect the 1^{st} harmonic with around 30 dB suppression and the 0^{th} harmonic in the central output waveguide with 20 dB suppression of other sidebands. The lower two waveguides collect the -1^{st} and -2^{nd} harmonic.

As previously mentioned, setting $\theta_s = 2\theta_\pi/(M+1)$ directs the harmonics above $(M+1)/2$ towards the outputs. For the example of the 16-by-5 star coupler, it means the output efficiently collects the 2^{nd} harmonic, collects also the -4^{th}, while the direction of the output collecting the 1^{st} harmonic coincides with the direction of the -5^{th} harmonic, ... In the example discussed in Fig. 4, this overlap does not significantly decrease the suppression rate because the modulation used doesn't contain substantial power in these overlapping harmonics. However, if we aim to use different modulations that contain considerable power in these higher harmonics, it could reduce the suppression ratio. Considering dual sine phase modulation as discussed in Fig. 4(j-l), the resulting collected output can be plotted as seen in Fig. 6. In this figure, we only plotted outputs 1,2 and 3 since, a symmetric comb profile and a symmetric star coupler design, outputs 4 and 5 can be derived through symmetry from outputs 2 and 3 by reversing the sign of the harmonics as can also be seen in the example from 5(d). From Fig. 6, it is evident that when $\theta_s = 2\theta_\pi/(M+1) = 2\theta_\pi/6$, indeed higher harmonics are overlapping when the collected harmonics are directed to the outputs. However, by choosing a slightly adjusted angular separation $\theta_s = 2\theta_\pi/(M+3/2) = 2\theta_\pi/(6+1/2)$, the higher harmonics are directed in between the various output angles. Figure 6, therefore shows that this slight change of the output angle is a mitigation strategy for overlapping harmonics.

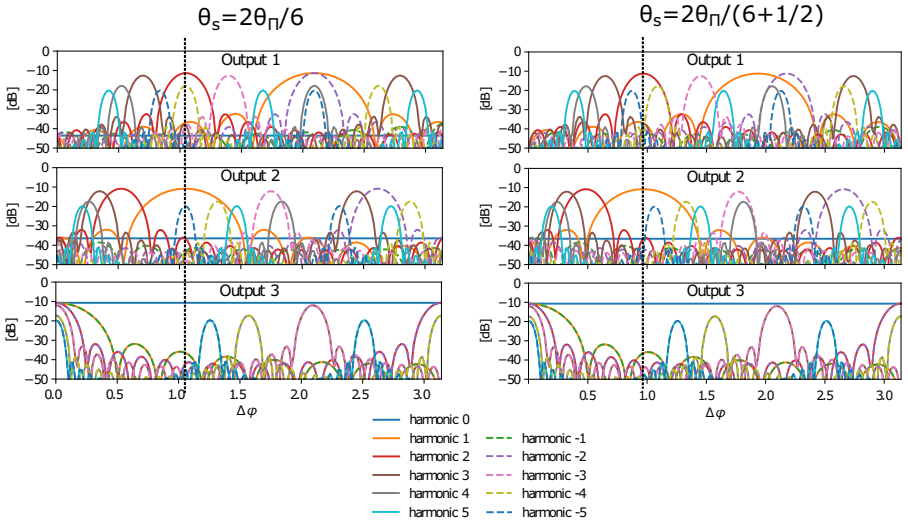

Fig. 6. The harmonic power collected by various outputs from the 16-by-5 star coupler for different output angles, under the assumption of a dual-sine phase modulation input, shows distinct characteristics. When $\theta_s = 2\theta_\pi/6$, the higher harmonics overlap as they are directed toward the outputs. On the other hand, when $\theta_s = 2\theta_\pi/(6+1/2)$, the higher harmonics are steered in between the outputs. This observation illustrates that by choosing suitable output angles, it is possible to mitigate the overlap of higher harmonics with the outputs, thus improving the suppression ratio.

IQ-based frequency shifters remove sidebands through destructive interference from arms with multiple modulators [42–44]. Assuming lossless phase modulation in each arm, they have an upper-limit device loss of −4.7 dB for collecting the 1^{st} harmonic while having non-negligible higher harmonics. When optimally modulating for the first harmonic, the IQ-based frequency

Optics EXPRESS

shifters exhibits a suppression ratio limited to approximately 15 dB due to the presence of -3^{rd} harmonics [13–15]. Improving the suppression ratio relative to this harmonic comes at a cost of power efficiency. Additionally, the insertion loss of individual modulators significantly impacts power efficiency. Recent demonstrations of IQ-based modulators show therefore largely varying suppression ratios of 10 to 25 dB and varying insertion losses [42,43] (e.g., a lithium-niobate-based IQ frequency shifter shows an insertion loss of around −17.6 dB and a suppression ratio of 22 dB [42]).

To compare the theoretical performance of the designed frequency shifter with the IQ-based frequency shifter, we therefore assume both employ identical lossless modulations. For this theoretical comparison, we also neglect propagation losses (usually below 2 dB/cm for 220 nm thick SOI [45]) and losses due to splitters for both types of frequency shifter (0.05–0.2 dB per 1×2 - splitter [45]). Assuming the same modulation, we can see that the 16-by-5 multi-beam frequency shifter requires 6 dB more RF power due to the multitude of modulators. When we look at the optical power budget, results from Fig. 5 show the collected power of the first harmonic of the 16-by-5 frequency shifter is −6.9 dB, which is less than the IQ-based frequency shifter (−4.7 dB). However, in the proposed design, we collect the light of other harmonics, resulting in a simulated optical loss of around −2.4 dB. This simulated value is primarily due to star coupler insertion losses, while the loss from uncollected higher harmonics is near zero because of the comb profile, which concentrates the power in the lower harmonics. In addition, we can see from Fig. 5(d) that for the 16-by-5 example of the multi-beam frequency shifter, simulations indicate around 30 dB suppression for the 1^{st} harmonic and 20 dB for the 0^{th} - and 2^{nd} harmonic. It's worth noting that the theoretical performance can be enhanced with more optimally designed star couplers. Previous demonstrations have shown that devices with superior suppression ratios and reduced insertion losses can be fabricated through optimization of mode matching and suppression of scattering in a star coupler [46].

5. Conclusion

In this paper, we introduced the theoretical framework for understanding the construction of multi-beam frequency shifters using an array of modulators and an FPR. By modulating the array in a periodic, wave-like manner, frequency-shifted beams can be generated and directed in different directions. Subsequently, we proposed using a star coupler to collect the light in different frequency-shifted beams on-chip. We also discussed design considerations and presented a simulation of a 16-by-5 star coupler-based multi-beam frequency shifter as an example. By using perfect sine phase modulators and tuning the delay between the consecutive modulators such that the five harmonics (2,-1,0,1,2) are directed to the five outputs, we simulated a suppression ratio of between 20 and 30 dB for the different outputs compared to other harmonics and with a simulated loss of −2.4 dB due to the star coupler. These simulation results illustrate the feasibility of our proposed multi-beam frequency shifter and highlight the potential for various photonic integrated devices that necessitate multiple frequency shifts.

Funding. Vlaamse regering (Methusalem grant (Roel Baets)).

Acknowledgments. The authors are grateful to Wim Bogaerts for giving access to the jupyter notebooks from the course 'Photonic Integrated Circuits' from Ghent University, which helped developing the design and simulation framework used in this paper.

Disclosures. The authors declare no conflicts of interest.

Data availability. Data underlying the results presented in this paper are not publicly available at this time but may be obtained from the authors upon reasonable request.

References

1. Y. Li, L. Marais, H. Khettab, Z. Quan, S. Aasmul, R. Leinders, R. Schüler, P. E. Morrissey, S. Greenwald, P. Segers, M. Vanslembrouck, R. M. Bruno, P. Boutouyrie, P. O'Brien, M. de Melis, and R. Baets, "Silicon photonics-based

Optics EXPRESS

laser doppler vibrometer array for carotid-femoral pulse wave velocity (pwv) measurement," Biomed. Opt. Express **11**(7), 3913 (2020).
2. V. Aranchuk, A. Lal, C. Hess, and J. Sabatier, "Multi-beam laser doppler vibrometer for landmine detection," Opt. Eng. **45**(10), 104302 (2006).
3. D. Francis, R. P. Tatam, and R. M. Groves, "Shearography technology and applications: A review," Meas. Sci. Technol. **21**(10), 102001 (2010).
4. B. Lengenfelder, F. Mehari, M. Hohmann, M. Heinlein, E. Chelales, M. J. Waldner, F. Klämpfl, Z. Zalevsky, and M. Schmidt, "Remote photoacoustic sensing using speckle-analysis," Sci. Rep. **9**(1), 1057 (2019).
5. B. Jalali and S. Fathpour, "Silicon photonics," J. Lightwave Technol. **24**(12), 4600–4615 (2006).
6. Y. Li, J. Zhu, M. Duperron, P. O'Brien, R. Schüler, S. Aasmul, M. de Melis, M. Kersemans, and R. Baets, "Six-beam homodyne laser doppler vibrometry based on silicon photonics technology," Opt. Express **26**(3), 3638–3645 (2018).
7. S. J. Rothberg, M. S. Allen, P. Castellini, D. D. Maio, J. J. Dirckx, D. J. Ewins, B. J. Halkon, P. Muyshondt, N. Paone, T. Ryan, H. Steger, E. P. Tomasini, S. Vanlanduit, and J. F. Vignola, "An international review of laser doppler vibrometry: Making light work of vibration measurement," Opt. Lasers Eng. **99**, 11–22 (2017).
8. D.-T. Jong and K. Hotate, "Frequency division multiplexing of optical fiber sensors using an optical delay loop with a frequency shifter," Appl. Opt. **28**(7), 1289–1297 (1989).
9. G. E. Sommargren, "Up/down frequency shifter for optical heterodyne interferometry," J. Opt. Soc. Am. **65**(8), 960–961 (1975).
10. J. L. Brooks, R. H. Wentworth, R. C. Youngquist, M. Tur, B. Y. Kim, and H. J. Shaw, "Coherence multiplexing of fiber-optic interferometric sensors," J. Lightwave Technol. **3**(5), 1062–1072 (1985).
11. L. M. Johnson and C. H. Cox, "Serrodyne optical frequency translation with high sideband suppression," J. Lightwave Technol. **6**(1), 109–112 (1988).
12. D. M. S. Johnson, J. M. Hogan, S.-w. Chiow, and M. A. Kasevich, "Broadband optical serrodyne frequency shifting," Opt. Lett. **35**(5), 745–747 (2010).
13. S. Shimotsu, S. Oikawa, T. Saitou, N. Mitsugi, K. Kubodera, T. Kawanishi, and M. Izutsu, "Single side-band modulation performance of a linbo3 integrated modulator consisting of four-phase modulator waveguides," IEEE Photonics Technol. Lett. **13**(4), 364–366 (2001).
14. A. A. Dorrington and R. Kuennemeyer, "Single sideband techniques for laser doppler velocimeter frequency offset," Opt. Eng. **42**(11), 3239–3256 (2003).
15. T. Sueta and S. Shikama, "Integrated optical ssb modulator/frequency shifter," IEEE J. Quantum Electron. **17**(11), 2225–2227 (1981).
16. C. E. M. Strauss, "Synthetic-array heterodyne detection: a single-element detector acts as an array," Opt. Lett. **19**(20), 1609–1611 (1994).
17. Y. Fu, M. Guo, and P. B. Phua, "Spatially encoded multibeam laser doppler vibrometry using a single photodetector," Opt. Lett. **35**(9), 1356–1358 (2010).
18. A. Kowel, "Acousto-optics-a review of fundamentals," Proc. IEEE **69**(1), 48–53 (1981).
19. A. Korpel and T.-C. Poon, "Explicit formalism for acousto-optic multiple plane-wave scattering," J. Opt. Soc. Am. **70**(7), 817–820 (1980).
20. L. Cai, A. Mahmoud, M. Khan, M. Mahmoud, T. Mukherjee, J. Bain, and G. Piazza, "Acousto-optical modulation of thin film lithium niobate waveguide devices," Photonics Res. **7**(9), 1003 (2019).
21. L. Wan, Z. Yang, W. Zhou, M. Wen, T. Feng, S. Zeng, D. Liu, H. Li, J. Pan, N. Zhu, W. Liu, and Z. Li, "Highly efficient acousto-optic modulation using nonsuspended thin-film lithium niobate-chalcogenide hybrid waveguides," Light: Sci. Appl. **11**(1), 145–7538 (2022).
22. M. M. D. Lima, M. Beck, R. Hey, and P. V. Santos, "Compact mach-zehnder acousto-optic modulator," Appl. Phys. Lett. **89**(12), 121104 (2006).
23. E. A. Kittlaus, W. M. Jones, P. T. Rakich, N. T. Otterstrom, R. E. Muller, and M. Rais-Zadeh, "Electrically driven acousto-optics and broadband non-reciprocity in silicon photonics," Nat. Photonics **15**(1), 43–52 (2021).
24. J. M. Lukens, H. H. Lu, B. Qi, P. Lougovski, A. M. Weiner, and B. P. Williams, "All-optical frequency processor for networking applications," J. Lightwave Technol. **38**(7), 1678–1687 (2020).
25. S. J. B. Yoo, "Wavelength conversion technologies for wdm network applications," J. Lightwave Technol. **14**(6), 955–966 (1996).
26. H. Tabatabai, D. E. Oliver, J. W. Rohrbaugh, and C. Papadopoulos, "Novel applications of laser doppler vibration measurements to medical imaging," Sens. Imaging **14**(1-2), 13–28 (2013).
27. C. P. Wang, "Laser doppler velocimetry," J. Quant. Spectrosc. Radiat. Transfer **40**(3), 309–319 (1988).
28. D. Marpaung, J. Yao, and J. Capmany, "Integrated microwave photonics," Nat. Photonics **13**(2), 80–90 (2019).
29. M. K. Smit and C. V. Dam, "Phasar-based wdm-devices: Principles, design and applications," IEEE J. Sel. Top. Quantum Electron. **2**(2), 236–250 (1996).
30. A. Rahim, A. Hermans, B. Wohlfeil, D. Petousi, B. Kuyken, D. V. Thourhout, and R. Baets, "Taking silicon photonics modulators to a higher performance level: State-of-the-art and a review of new technologies," Adv. Photonics **3**(02), 024003 (2021).
31. G. Sinatkas, T. Christopoulos, O. Tsilipakos, and E. E. Kriezis, "Electro-optic modulation in integrated photonics," J. Appl. Phys. **130**(1), 010901 (2021).
32. R. A. Soref and B. R. Bennett, "Electrooptical effects in silicon," IEEE J. Quantum Electron. **23**(1), 123–129 (1987).

Optics EXPRESS

33. Q. Chang, J. Gao, and Y. Su, "Generation of optical comb frequency signal with high spectral flatness using two cascaded optical modulators," *Asia Optical Fiber Communication and Optoelectronic Exposition and Conference* pp. 1–3 (2008).
34. S. Ozharar, F. Quinlan, I. Ozdur, S. Gee, and P. J. Delfyett, "Ultraflat optical comb generation by phase-only modulation of continuous-wave light," IEEE Photonics Technol. Lett. **20**(1), 36–38 (2008).
35. J. He, T. Dong, and Y. Xu, "Review of photonic integrated optical phased arrays for space optical communication," IEEE Access **8**, 188284–188298 (2020).
36. W. Xu, L. Zhou, L. Lu, and J. Chen, "Aliasing-free optical phased array beam-steering with a plateau envelope," Opt. Express **27**(3), 3354 (2019).
37. W. Bogaerts, M. Fiers, M. Sivilotti, and P. Dumon, "The ipkiss photonic design framework," *Optical Fiber Communication Conference* p. W1E.1 (2016).
38. P. Bienstman and R. Baets, "Optical modelling of photonic crystals and vcsels using eigenmode expansion and perfectly matched layers," Opt. Quantum Electron. **33**(4/5), 327–341 (2001).
39. A. Rahim, J. Goyvaerts, and B. Szelag, *et al.*, "Open-access silicon photonics platforms in europe," IEEE J. Sel. Top. Quantum Electron. **25**(5), 1–18 (2019).
40. M. Gehl, D. Trotter, A. Starbuck, A. Pomerene, A. L. Lentine, C. Derose, W. Wang, R. L. Davis, T. J. Jung, R. Lodenkamper, L. J. Lembo, J. C. Brock, and M. C. Wu, "Active phase correction of high resolution silicon photonic arrayed waveguide gratings," Opt. Express **25**(6), 6320–6334 (2017).
41. M. Jacques, A. Samani, E. El-Fiky, D. Patel, Z. Xing, and D. V. Plant, "Optimization of thermo-optic phase-shifter design and mitigation of thermal crosstalk on the soi platform," Opt. Express **27**(8), 10456 (2019).
42. H.-P. Lo and H. Takesue, "Precise tuning of single-photon frequency using an optical single sideband modulator," Optica **4**(8), 919 (2017).
43. P. Shi, L. Lu, C. Liu, G. Zhou, W. Xu, J. Chen, and L. Zhou, "Optical fmcw signal generation using a silicon dual-parallel mach-zehnder modulator," IEEE Photonics Technol. Lett. **33**(6), 301–304 (2021).
44. M. Xu, M. He, H. Zhang, J. Jian, Y. Pan, X. Liu, L. Chen, X. Meng, H. Chen, Z. Li, X. Xiao, S. Yu, S. Yu, and X. Cai, "High-performance coherent optical modulators based on thin-film lithium niobate platform," Nat. Commun. **11**(1), 1 (2020).
45. W. Bogaerts, D. Pérez, J. Capmany, D. A. Miller, J. Poon, D. Englund, F. Morichetti, and A. Melloni, "Programmable photonic circuits," Nature **586**(7828), 207–216 (2020).
46. J. Park, G. Kim, H. Park, J. Joo, S. Kim, and M.-J. Kwack, "Performance improvement in silicon arrayed waveguide grating by suppression of scattering near the boundary of a star coupler," Appl. Opt. **54**(17), 5597 (2015).